

Supporting Information: Computational investigation of the kinetics and mechanism of the initial steps of the Fischer-Tropsch Synthesis on Cobalt

Pieter van Helden,^{*a} Jan-Albert van den Berg,^a Melissa A. Petersen,^a Werner Janse van Rensburg,^{a‡} Ionel M. Ciobîcă,^b and Jan van de Loosdrecht^a

1 Calculation of partition functions

To be able to calculate the temperature dependent corrections to the enthalpy, entropy and free energy values of each species, the partition function of each species needs to be known. This can be calculated using the approximation:

$$q_i = q_{i,\text{vib}}q_{i,\text{rot}}q_{i,\text{trans}}$$

where $q_{i,\text{vib}}$ is the partition function due to vibrational motions, $q_{i,\text{rot}}$ is the partition function due to rotational motions and $q_{i,\text{trans}}$ is the partition function due to the translation motion.

1.1 Vibrational partition function

The calculation of the vibrational partition function $q_{i,\text{vib}}$ is simplest within the harmonic oscillator approximation. The energy-levels of an harmonic oscillator can be calculated from quantum mechanics and, assuming the particle has $3N - 6$ vibrational modes (ν_i), the partition function can be expressed as:

$$q_{i,\text{vib}} = \prod_{i=1}^{3N-6} \frac{1}{1 - e^{-h\nu_i/k_B T}}$$

where h is the Planck constant, k_B the Boltzmann constant and T is the temperature.

1.2 Free rotation and translation

The free rotational partition function, $q_{i,\text{rot}}$, is estimated from the energy eigenstates of the Schrödinger equation that describes rotation of a free particle. The exact form of the equation within the harmonic approximation depends on whether the species is a linear or a spherically symmetric rotor, or in general an asymmetric rotor. For a linear rotor the quantum partition function is the sum over energy states J in the form

$$q_{i,\text{lin,rot}} = \sum_{J=0}^{\infty} (2J+1) e^{-\frac{J(J+1)}{\Theta_{\text{lin,rot}}}}, J = 0, 1, 2, \dots$$

where the rotational temperature $\Theta_{\text{lin,rot}} = \frac{2Ik_B T}{h^2}$ and I is the moment of inertia. In the classical limit the states can be considered to be nearly continuous and thus the sum can be replaced by an integral:

$$q_{i,\text{lin,rot}}^{\text{clas}} = \int_0^{\infty} (2J+1) e^{-\frac{J(J+1)}{\Theta_{\text{lin,rot}}}} dJ = \Theta_{\text{lin,rot}}$$

Before continuing, note that for centrosymmetric linear rotors the symmetry number (σ) must be included. Since non-centrosymmetric linear rotors have symmetry number $\sigma = 1$ we have in general

$$q_{i,\text{lin,rot}}^{\text{clas}} = \Theta_{\text{lin,rot}} / \sigma$$

^a Sasol, Group Technology, P.O. Box 1, Sasolburg 1947, South Africa, E-mail: pieter.vanhelden@sasol.com

^b Sasol Technology Netherlands B.V., Vlierstraat 111, 7544 GG Enschede, The Netherlands

[‡] Present address: Centre for High Performance Computing, 15 Lower Hope Road, Rosebank, Cape Town, South Africa, 7700

For a spherically symmetric rotor a similar approach can be followed leading to the formulation:

$$q_{i,\text{spher,rot}} = \sum_{J=0}^{\infty} (2J+1)^2 e^{-\frac{J(J+1)}{\Theta_{\text{spher,rot}}}}, J = 0, 1, 2, \dots$$

In the classical limit this reduces to:

$$q_{i,\text{spher,rot}}^{\text{clas}} \approx \sqrt{\pi(\Theta_{\text{spher,rot}})^3} / \sigma$$

In the present microkinetic model the quantum formulations were used by applying an asymptotic expansion based on the Euler-Mclaurin series. To maintain accuracy the Euler-Mclaurin series was truncated only after 20 terms in the actual code implementation. Aside from linear rotors, the spherically symmetric rotors (of which CH₄ is an example) can also be expressed in a form that can be represented exactly using a similar approach as the one thus far outlined. If a species is neither linear nor spherically symmetric, we use a quasi-spherically symmetric approximation by rescaling, setting $I_A = I_B = I_C = \sqrt[3]{I_A I_B I_C}$.

The free translational partition function is calculated by summing over the energies of the eigenstates of the Schrödinger equation for a free particle. Along one dimension this is given by:

$$q_{\text{trans}}^{\text{1D}} = \sum_{x=1}^{\infty} e^{-\frac{h^2 x^2}{8m_i k_B T l^2}}$$

Once again the translational temperature $\Theta_{i,\text{trans}} = 2\pi m_i k_B T / h^2$ can be used, giving

$$q_{\text{trans}}^{\text{1D}} = \sum_{x=1}^{\infty} e^{-\frac{x^2}{4\pi l^2 \Theta_{i,\text{trans}}}}$$

where m_i is the mass and l is the translational length of the dimension. In the classical limit the sum is replaced by an integral giving

$$q_{\text{trans}}^{\text{1D,clas}} = \int_{x=0}^{\infty} e^{-\frac{x^2}{4\pi l^2 \Theta_{i,\text{trans}}}} dx = l \sqrt{\Theta_{i,\text{trans}}}$$

The calculation of the exact translational partition function can be achieved by applying an asymptotic expansion based on the Euler-Mclaurin series. To maintain accuracy the Euler-Mclaurin series was truncated only after 16 terms in the actual code implementation. The direct sum is implemented for $4\pi l^2 \Theta_{i,\text{trans}} < 1.535$ because, interestingly, the Euler-Mclaurin series terminates in this case, such that the asymptotic expansion just evaluates to

$$q_{\text{trans}}^{\text{1D}}(\Theta_{i,\text{trans}}) = q_{\text{trans}}^{\text{1D,clas}}(\Theta_{i,\text{trans}}) + 1/2$$

1.3 Partition function of species with frustrated motions

On surface sites the translational and rotational mobility of a species will depend on the energy landscape it experiences. These motions can be considered to take place within an energy potential. Due to the periodicity of rotation and translation over a surface lattice the frustrated motions will be represented by a particle in motion in a cosine potential well. In *kinsolv* the implemented formulation of a frustrated rotation partition function follows the approach given by McClurg et al.¹ To calculate these values a vibrational frequency that represents the frustrated rotation, along with a rotational barrier should be provided. Hindered translational motions can also be described using potential functions that are sums of cosine-potentials, with each cosine-potential along a specific dimension. The implementation for frustrated rotations can directly be applied to hindered translations by noting that the vibrational frequencies that are used in this case should relate to the translational motions.

1.4 Linking sticking probability to partition functions

Adsorption transition states are described by a 2D free translating gas over the active site area. Although this ensures thermodynamic consistency, it might overestimate the actual adsorption rates of these gases. Since the usual Collision Theory approach that is frequently used in microkinetic models is not thermodynamically consistent,² we decided to rather include an ad hoc correction scheme to the transition state species in the *kinsolv* program that is akin to the notion of sticking probabilities. This is similar to the collision theory approach, while maintaining thermodynamic consistency.

The sticking probability is the ratio

$$P_{\text{stick}}(\theta, T) = \frac{N_{\text{stick}}}{N_{\text{impinge}}}$$

where N_{stick} is the number of particles that stick to a surface area per second and N_{impinge} is the number of particles that impinge with the same surface area per second. If $P_{\text{stick}} < 1$ it implies that some of the gas species were repelled back to the gas phase by the local energy landscape at the transition state. In the most general sense, the sticking probability is a function of temperature and coverage. The sticking probability at some temperature in the limit of zero coverage is then $S_0(T) = P_{\text{stick}}(0, T)$. In the correction scheme applied within *kinsolv*, the sticking probability is assumed to affect the partition function of the transition state directly, and it thus behaves as an attenuation factor:

$$\dot{q}_{TS,i} = q_{i,\text{vib}}q_{i,\text{rot}}q_{i,\text{trans}} \cdot P_{\text{stick}}(\theta, T) \approx q_{i,\text{vib}}q_{i,\text{rot}}q_{i,\text{trans}} \cdot S_0$$

The effective free energy of the transition state thus increases as P_{stick} decreases to zero.

For species such as CO* and ethylene S_0 is close to unity, while for H₂ a value of $S_0 = 0.03$ is used (experimental value ranges between 0.01 and 0.05)³ for the terrace-like sites and a value close to unity for the step site. For paraffin products like CH₄ and ethane, S_0 is usually very small and a value of 10⁻⁶ was therefore used.

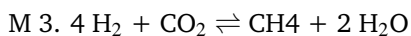
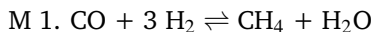
2 Thermochemical correction to gas phase species

It is essential for an overall good description of the chemistry to ensure the overall gas phase thermodynamics is correct. If this is not the case, any equilibrium process will be incorrectly described, as well as gas to surface adsorption and desorption processes. The overall thermodynamics for the reactions described here is well studied and the DFT results can be checked and corrected in respect to these.

It must be noted that there is a known inherent problem in DFT in calculating the electronic state of CO.^{4,5} Calculated CO adsorption energies can be incorrect relative to the experiment, with deviations of between 0.15 eV and 0.50 eV. If the calculated electronic energy of CO is used as is, there is a mismatch in the overall thermodynamics of all the gas phase reactions involving CO, as well as resulting in overestimated adsorption energies. An in-depth discussion of the origins of this effect is outside the scope of the current work. However, it implies that we need to correct the energy level of the gas phase CO molecule. By using the DFT calculated gas phase enthalpies and free energies, the energies of the gas phase species can be adapted to ensure that the resulting temperature dependent curves agree with the experimental values. A thermochemical correction of -0.49 eV was applied to the CO gas phase electronic energy to improve the agreement with the experimental enthalpies.

To obtain the correct Gibbs free energy dependence on temperature for the gas phase species, the calculation of the entropy contribution is very important. This is done by calculating the number of states accessible to the molecule at a given temperature (partition functions). We have compared a number of experimentally observed accessible states of the gas phase molecules,⁶ with the corresponding calculated partition functions in *kinsolv*. The individually computed partition functions of most of the gas phase molecules (CO, H₂, CO₂) are in good agreement with experimental partition functions in relevant temperature ranges. However, the roto-vibrational partition function of H₂O and CH₄ were somewhat less accurate. A correction was applied to obtain a better experimental agreement. The H₂O molecule is an asymmetric top when it comes to rotation. The quasi-spherical approach in *kinsolv* seems to result in too few states (see Figure 1). The approximately correct number of roto-vibrational states can be obtained by changing the symmetry number of H₂O to the value of $\sigma \approx 0.25$ (four times more states than the calculated unsymmetrical value). The methanation reaction (M1, see below) was chosen as a test case since it is a representative and typical reaction which forms part of the Fischer-Tropsch process. The recalculated thermodynamics of the methanation process with the correction applied to H₂, can be seen in Figure 2. By changing the water symmetry number, a better agreement between the calculated and experimental values is obtained. In a similar manner the apparent symmetry number for CH₄ of 0.75 was obtained. Other gas phase corrections: C₂H₄ $\sigma = 0.125$ and E_0 corrected by -0.161 eV. C₂H₆ $\sigma = 0.08$ and no E_0 correction was needed.

The calculated overall thermodynamics of the gas molecules were compared to the experimental overall gas phase thermodynamics of four relevant reactions involved in the methanation reaction:



M 4. $\text{CO} + \text{H}_2\text{O} \rightleftharpoons \text{CO}_2 + \text{H}_2$

For all the species involved the corrected DFT calculated energies, vibrational frequencies and moments of inertia were used. The comparison of our calculated thermodynamic values to the experimental values can be seen in Figure 3. From this figure it is clear that the reaction enthalpies and their temperature dependence are accurately described by *kinsolv* up to 1000 K. The Gibbs free energy changes are very sensitive to the entropy values. Despite this we obtain a very good agreement with the experimental values up to 1000 K. Note reaction M 4 (which does not contain CH_4) corresponds the best with experiment. The slight mismatch of the reaction containing CH_4 indicates that there is still a small level of uncertainty which lies within the calculation of the CH_4 partition function. The agreement with the experiment is good enough to validate the gas phase values used in the microkinetic model implementation. In a similar manner the C_2 gas species were also corrected to ensure a good agreement with the experimental thermodynamics.

3 Coverage dependence of CO^* on $\text{Co}(100)$

The energy values for CO^* on $\text{Co}(100)$ were calculated using plane-wave periodic boundary condition Density Functional Theory (DFT). The DFT calculations used were performed with the Vienna *ab initio* Simulation Package (VASP)⁷⁻⁹ using plane waves and ultrasoft pseudopotentials (US-PP).^{10,11} All energies were calculated using the generalized spin-polarized gradient approximation (GGA) with the Perdew and Wang exchange-correlation functional (GGA-PW91).¹² The electron distribution at the Fermi level was modelled by Methfessel and Paxton¹³ smearing with $\sigma = 0.2$ eV. The cut-off energy for the calculations was set to 400 eV and dipole corrections were applied. A FCC $\text{Co}(100)$ surface model with 4 layers, with a 10 Å vacuum layer was used. A $p(3 \times 3)$ surface unit cell was used for the calculations and the k -point sampling was generated by following the Monkhorst-Pack¹⁴ procedure on a $4 \times 4 \times 1$ mesh. Partial Hessian vibrational analysis was performed on the calculated structures. From these calculations we obtained the vibrational frequencies (ν_i) within the harmonic approximation. From the list of frequencies the vibrational zero-point energy was calculated $E_{\text{ZPVE}} = \frac{1}{2} \sum_i h\nu_i$, with h as the Planck constant.

The number of CO molecules in the unit cells was systematically increased from 1 to 9 to obtain a coverage dependent adsorption energy curve. The resulting curve can be seen in Figure 4.

4 CO desorption profile on $\text{Co}(111)$

Two cases for the description of CO adsorption energies were initially considered on Site-A/ $\text{Co}(111)$. In the first, a constant adsorption energy (about 1.26 eV) was used. In the second case the energy of CO on the $\text{Co}(111)$ surface was made coverage dependent. This coverage dependent CO adsorption energy profile was extracted from two sources. The first profile was extracted from Lahtinen et al.¹⁵ who performed detailed studies on CO desorption. Using the temperature programmed desorption (TPD) spectrum, a coverage dependent CO desorption energy profile was constructed assuming a saturation coverage of 0.60 ML. The second source was desorption data based on previous in-house surface science experiments.¹⁶

The coverage dependent CO adsorption energies can be seen in Figure 5. The resulting comparison of CO^* coverages using these three approaches during a TPD (at $2 \text{ K}\cdot\text{s}^{-1}$ ramp rate and 1×10^{-7} mbar CO) simulated with *kinsolv* can be seen in Figure 5. It is clear that the use of a constant adsorption energy results in a very different behaviour of the model compared to the coverage dependent profiles. A constant value would result in a too large CO coverage and an incorrect desorption peak. The result for the TPD trace using the coverage dependent energy based on our in-house work¹⁶ is compared to the experimental ultra-high vacuum $\text{Co}(0001)$ CO TPD trace¹⁵ in Figure 6. The resulting TPD trace for CO corresponds well with the experimental TPD.

Similar efforts were made to ensure the description of H^* is correct. The simulated TPD traces of H^* desorption correspond well to the experimental results. These have been reported earlier.³

5 Descriptor for C_2 formation selectivity

A comparative selectivity descriptor value is used to assess whether the microkinetic model is producing a sufficiently meaningful amount of C_2 products compared to what is experimentally expected. To do this we use a C_2 to C_1 C atom-based ratio:

$$\dot{S} = \frac{2r_{\text{C}_2}}{r_{\text{C}_1}}$$

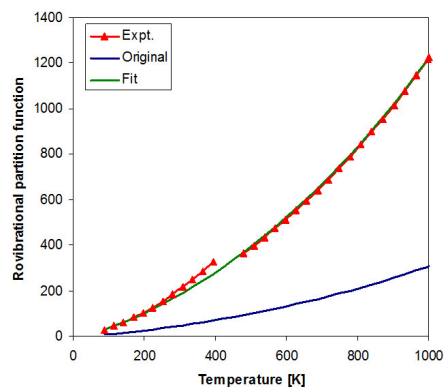


Fig. 1 Calculated, fitted and experimental roto-vibrational partition function of H₂O

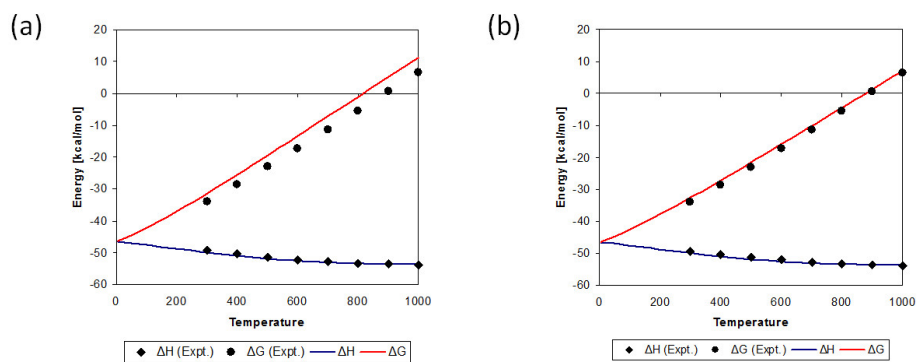


Fig. 2 Comparison of experimental and calculated thermodynamic values at various H₂O symmetries. (a) $\sigma = 2$ (b) $\sigma = 0.25$

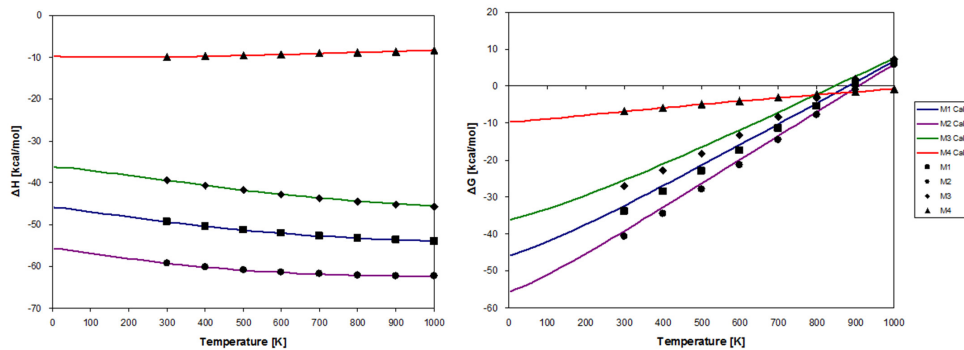


Fig. 3 Comparison of calculated and experimental reaction enthalpies (left) and Gibbs free energies (right) of reactions M1–M4 as a function of reaction temperature.

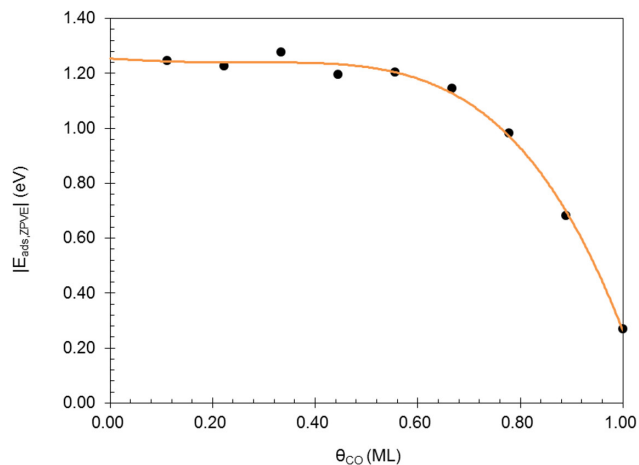


Fig. 4 Calculated adsorption energies of CO* on Co(100) as a function of coverage (black). Orange line indicates fitted function used.

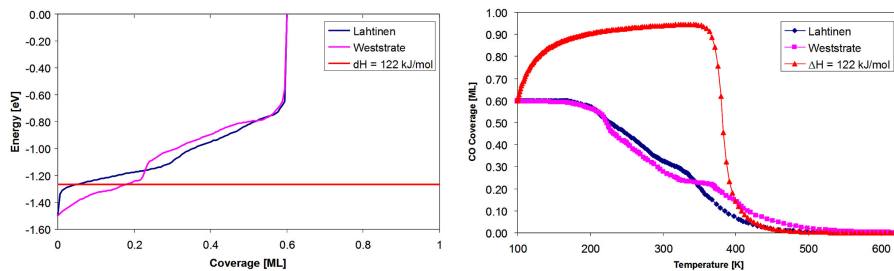


Fig. 5 Coverage dependent adsorption energies from various sources (left) and the corresponding simulated CO* coverage during a TPD at 10^{-7} mbar CO (right)

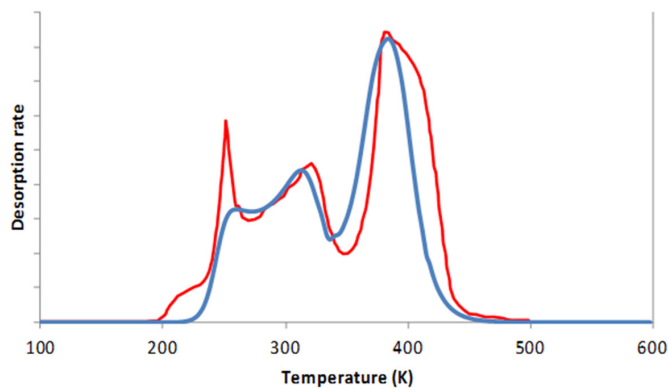


Fig. 6 TPD traces of CO on the Co(111) model. The microkinetic model trace (blue) and the experimental trace on Co(0001)¹⁵ (red).

where r_{C_2} is the sum total TOF of C_2 production and r_{C_1} is the TOF of methane production. The expected values of \acute{S} , as derived from a variety of experiments,^{17–27} vary depending on the catalyst preparation and the reaction conditions, but it ranges typically between 0.1 and 0.3 with a mean around 0.15. The summary of the data set used is shown in Table 1.

Table 1 Summary of \acute{S} values obtained from a selection of experimental FTS product distributions

Year	Reference	T (K)	P_{total}	$H_2:CO$	χ_{CO}	\acute{S}	Catalyst ^a
1989	Satterfield ¹⁷	493	11.8	1.6	11–70	0.257	Co/SiO ₂ /MgO
1989	Satterfield ¹⁷	503	7.9	1.5	11–70	0.291	Co/SiO ₂ /MgO
1993	Iglesia et al. ¹⁸	473	20	2.0	9.5	0.200	Co/TiO ₂
1994	Van Berge ¹⁹	495	4	1.7		0.202	Co/Al ₂ O ₃ /Re
1994	Van Berge ¹⁹	495	20	1.7		0.129	Co/Al ₂ O ₃ /Re
1997	Claeys ²⁰	463	8.4	2.3		0.159	Co/SiO ₂ /ZrO ₂
1997	Iglesia ²¹	473	20	2.05	55–65	0.102	Co/SiO ₂
1997	Iglesia ²¹	473	20	2.05	55–65	0.100	Co/TiO ₂
1997	Iglesia ²¹	473	20	2.05	55–65	0.150	Co/Al ₂ O ₃
2003	Zwane ²²	493	20	2.0		0.226	Co/Al ₂ O ₃ /V ₂ O ₅
2004	Dry ²³	493	20			0.210	Supported Co
2004	Dry ²³	503				0.175	Supported Co
2004	Dry ²³	503				0.226	Supported Co
2009	Bertoncini et al. ²⁴	503	20	2.0	56	0.140	Co/Al ₂ O ₃
2011	Visconti et al. ²⁵	503	20	2.1		0.134	Supported Co
2014	Todic et al. ²⁶	766	15–25	1.4–2.1	26–57	0.106–0.145	Co/Al ₂ O ₃ /Re
2014	Todic et al. ²⁶	751	15	1.4–2.1	18–62	0.095–0.189	Co/Al ₂ O ₃ /Re
2014	Todic et al. ²⁶	776	15–25	1.4–2.1	16–53	0.109–0.156	Co/Al ₂ O ₃ /Re
2015	Kasht et al. ²⁷	513	20	2	58	0.149	Co/Al ₂ O ₃
2015	Kasht et al. ²⁷	513	65	2	70	0.191	Co/Al ₂ O ₃
					Mean	0.148	
					Min.	0.095	
					Max.	0.291	

^a Catalyst formulation format "Co/Support/Promoter"

References

- 1 R. McClurg, R. Flagan and W. Goddard III, *J. Chem. Phys.*, 1997, **106**, 6675–6680.
- 2 I. Chorkendorff and J. W. Niemantsverdriet, *Concepts of Modern Catalysis and Kinetics*, Wiley-VCH, Weinheim, 2007.
- 3 P. van Helden, J.-A. van den Berg and C. J. Weststrate, *ACS. Catal.*, 2012, **2**, 1097–1107.
- 4 S. E. Mason, I. Grinberg and A. M. Rappe, *Phys. Rev. B*, 2004, **69**, 161401.
- 5 F. Abild-Pedersen and M. P. Andersson, *Surf. Sci.*, 2007, **601**, 1747.
- 6 L. Rothman, A. Barbe, D. C. Benner, L. Brown, C. Camy-Peyret, M. Carleer, K. Chance, C. Clerbaux, V. Dana, V. Devi, A. Fayt, J.-M. Flaud, R. Gamache, A. Goldman, D. Jacquemart, K. Jucks, W. Lafferty, J.-Y. Mandin, S. Massie and V. Nemtchi, *Journal of Quantitative Spectroscopy and Radiative Transfer*, 2003, **82**, 5.
- 7 G. Kresse and J. Hafner, *Phys. Rev. B*, 1993, **47**, 558–561.
- 8 G. Kresse and J. Furthmüller, *Phys. Rev. B*, 1996, **54**, 11169–11186.
- 9 G. Kresse and J. Furthmüller, *Comp. Mat. Sci.*, 1996, **6**, 15–50.
- 10 D. Vanderbilt, *Phys. Rev. B*, 1990, **41**, 7892–7895.
- 11 G. Kresse and J. Hafner, *J. Phys.: Condens. Matter*, 1994, **6**, 8245.
- 12 J. P. Perdew and Y. Wang, *Phys. Rev. B*, 1992, **45**, 13244.
- 13 M. Methfessel and A. T. Paxton, *Phys. Rev. B*, 1989, **40**, 3616.
- 14 H. J. Monkhorst and J. D. Pack, *Phys. Rev. B*, 1976, **13**, 5188.
- 15 J. Lahtinen, J. Vaari and K. Kauraala, *Surf. Sci.*, 1998, **418**, 502.
- 16 C. J. Weststrate, P. van Helden, J. van de Loosdrecht and J. W. Niemantsverdriet, *Surf. Sci.*, 2016, **648**, 60–66.
- 17 C. N. Satterfield, Indirect Liquefaction Contractor's Review Meeting Proceedings, 1989, pp. 125–155.
- 18 E. Iglesia, S. Reyes, R. Madon and S. Soled, *Adv. Catal.*, 1993, **39**, 221.
- 19 P. J. van Berge, *PhD thesis*, Potchefstroom University for Christian Higher Education, 1994.
- 20 M. Claeys, *PhD thesis*, University of Karlsruhe, 1997.
- 21 E. Iglesia, *Appl. Catal. A*, 1997, **161**, 59–78.

- 22 S. Zwane, *MSc thesis*, University of Cape Town, 2003.
- 23 M. Dry, *Fischer-Tropsch Technology*, Elsevier, 2004, vol. 152, ch. 3.
- 24 F. Bertoncini, M. Marion, N. Brodusch and S. Esnault, *Oil & Gas Science and Technology – Rev. IFP*, 2009, **64**, 79–90.
- 25 C. G. Visconti, E. Tronconi, L. Lietti, P. Forzatti, S. Rossini and R. Zennaro, *Topics in Catalysis*, 2011, **54**, 786–800.
- 26 B. Todic, W. Ma, G. Jacobs, B. H. Davis and D. B. Bukur, *J. Catal.*, 2014, **311**, 325–338.
- 27 A. Kasht, R. Hussain, M. Ghouri, J. Blank and N. O. Elbashir, *American Journal of Analytical Chemistry*, 2015, **6**, 659–676.

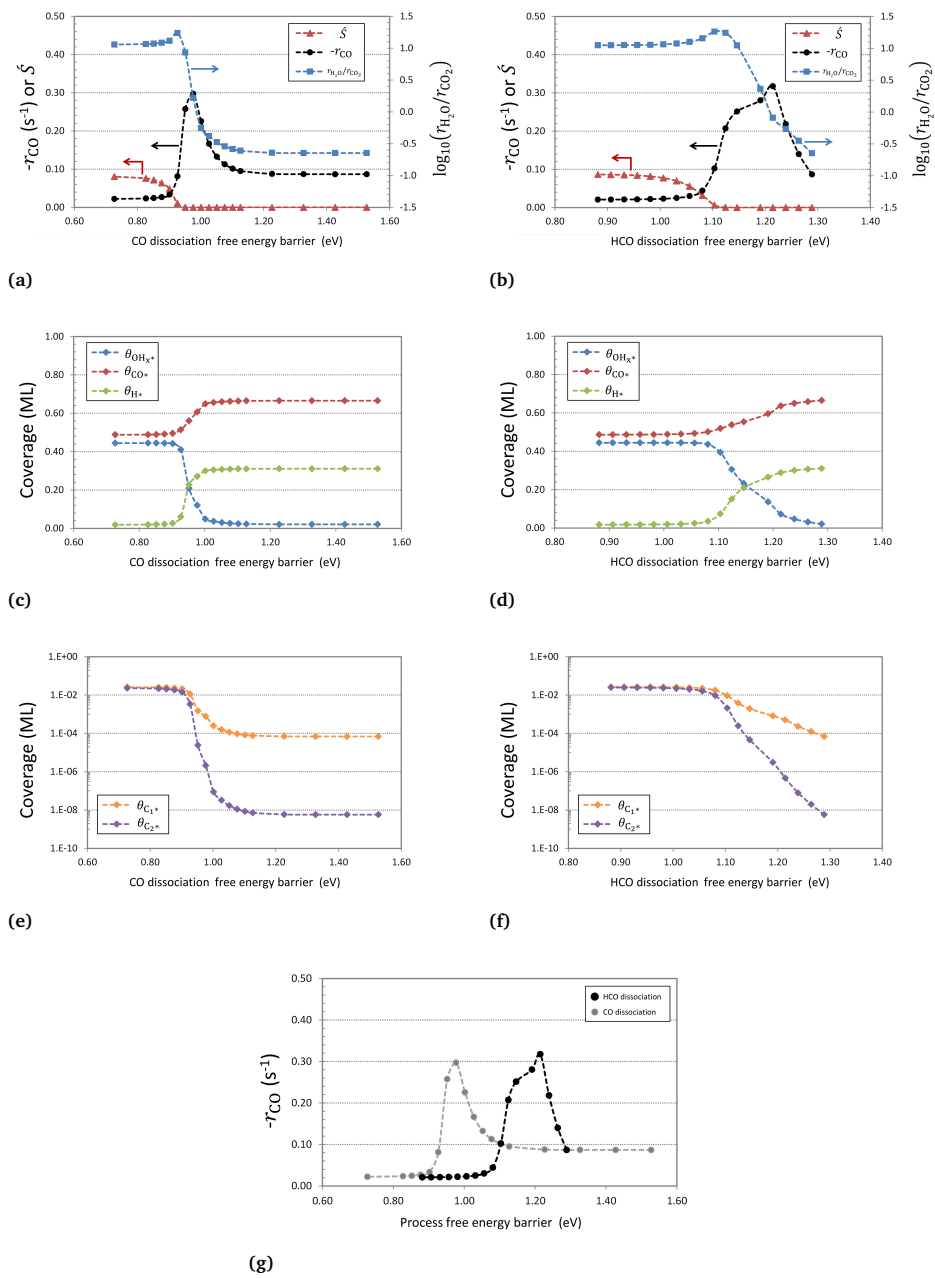


Fig. 7 Results of lowering the barriers for the CO scission process on Site-C: (a),(b) CO consumption rate, \dot{S} and the water production capacity; (c),(d) the total OH_x^* , CO^* and H^* coverages on all three sites; (e),(f) total C_1^* and C_2^* coverages. Results for the lowered CO dissociation barrier in (a,c,e) and lowered HCO dissociation barrier (b,d,f), respectively; (g) shows the comparison of the CO consumption rate curves.

Table 2 Outputs of the microkinetic analysis of the combined multi-site model at the reference conditions ($T = 503$ K; $P_{total} = 20$ bar; Inlet $H_2:CO = 2$; $\chi_{CO} = 50\%$) for scenario S2

Response	Value	Unit	
r_{CO}	-0.035	s^{-1}	
r_{CH_4}	0.031	s^{-1}	
r_{C_2}	0.001	s^{-1}	
\dot{S}	0.071		
S_{CH_4}	89	C-%	
S_{CO_2}	5	C-%	
Coverages (ML)	Site-A	Site-B	Site-C
θ_s^a	0.670	0.180	0.150
θ_{CO}	0.394	0.086	0.009
θ_H	0.023	8.39×10^{-6}	6.40×10^{-6}
θ_{HCO}	2.62×10^{-8}	5.64×10^{-7}	2.68×10^{-8}
θ_{COH}	2.80×10^{-8}	1.08×10^{-8}	2.07×10^{-10}
θ_C	2.47×10^{-10}	0.021	9.56×10^{-6}
θ_{CH}	4.63×10^{-5}	0.006	1.19×10^{-5}
θ_{CH_2}	1.24×10^{-7}	3.92×10^{-8}	3.19×10^{-9}
θ_{CH_3}	5.20×10^{-5}	4.74×10^{-9}	7.40×10^{-6}
θ_O	0.234	0.059	0.022
θ_{OH}	5.58×10^{-4}	9.49×10^{-5}	0.119
θ_{C_2}	0.017	0.007	1.56×10^{-4}
θ_*	6.51×10^{-4}	4.54×10^{-7}	6.75×10^{-8}

^a Initial amount of empty sites included in the model

Table 3 Outputs of the microkinetic analysis of the combined multi-site model at the reference conditions ($T = 503$ K; $P_{total} = 20$ bar; Inlet $H_2:CO = 2$; $\chi_{CO} = 50\%$) for scenario S3

Response	Value	Unit	
r_{CO}	-0.051	s^{-1}	
r_{CH_4}	0.046	s^{-1}	
r_{C_2}	0.001	s^{-1}	
\dot{S}	0.045		
S_{CH_4}	92	C-%	
S_{CO_2}	4	C-%	
Coverages (ML)	Site-A	Site-B	Site-C
θ_s^a	0.670	0.180	0.150
θ_{CO}	0.394	0.091	0.010
θ_H	0.032	1.22×10^{-5}	8.19×10^{-6}
θ_{HCO}	3.68×10^{-8}	8.23×10^{-7}	3.42×10^{-8}
θ_{COH}	3.93×10^{-8}	1.12×10^{-8}	2.64×10^{-10}
θ_C	1.94×10^{-10}	0.017	7.07×10^{-6}
θ_{CH}	4.13×10^{-5}	0.005	1.11×10^{-5}
θ_{CH_2}	1.25×10^{-7}	4.10×10^{-8}	3.16×10^{-9}
θ_{CH_3}	5.91×10^{-5}	5.60×10^{-9}	7.83×10^{-6}
θ_O	0.231	0.061	0.019
θ_{OH}	6.20×10^{-4}	1.10×10^{-5}	0.120
θ_{C_2}	0.011	0.005	6.64×10^{-5}
θ_*	8.06×10^{-4}	5.83×10^{-7}	7.59×10^{-8}

^a Initial amount of empty sites included in the model

Table 4 Outputs of the microkinetic analysis of the combined multi-site model at the reference conditions ($T = 503$ K; $P_{total} = 20$ bar; Inlet $H_2:CO = 2$; $\chi_{CO} = 50\%$) for scenario S4

Response	Value	Unit
r_{CO}	-0.028	s^{-1}
r_{CH_4}	0.023	s^{-1}
r_{C_2}	0.001	s^{-1}
\dot{S}	0.113	
S_{CH_4}	79	C-%
S_{CO_2}	12	C-%

Coverages (ML)	Site-A	Site-B	Site-C
θ_s^a	0.670	0.180	0.150
θ_{CO}	0.396	0.123	0.075
θ_H	0.270	0.002	6.14×10^{-4}
θ_{HCO}	4.30×10^{-7}	1.16×10^{-4}	2.47×10^{-6}
θ_{COH}	4.60×10^{-7}	9.35×10^{-7}	1.91×10^{-8}
θ_C	2.27×10^{-15}	1.07×10^{-6}	1.08×10^{-6}
θ_{CH}	1.49×10^{-5}	1.67×10^{-5}	1.67×10^{-5}
θ_{CH_2}	1.39×10^{-10}	1.12×10^{-11}	1.13×10^{-11}
θ_{CH_3}	1.99×10^{-10}	1.40×10^{-10}	1.40×10^{-10}
θ_O	0.002	0.007	0.001
θ_{OH}	6.13×10^{-5}	1.31×10^{-5}	0.073
θ_{C_2}	3.81×10^{-4}	0.016	8.14×10^{-8}
θ_*	9.89×10^{-4}	8.64×10^{-6}	5.75×10^{-7}

^a Initial amount of empty sites included in the model

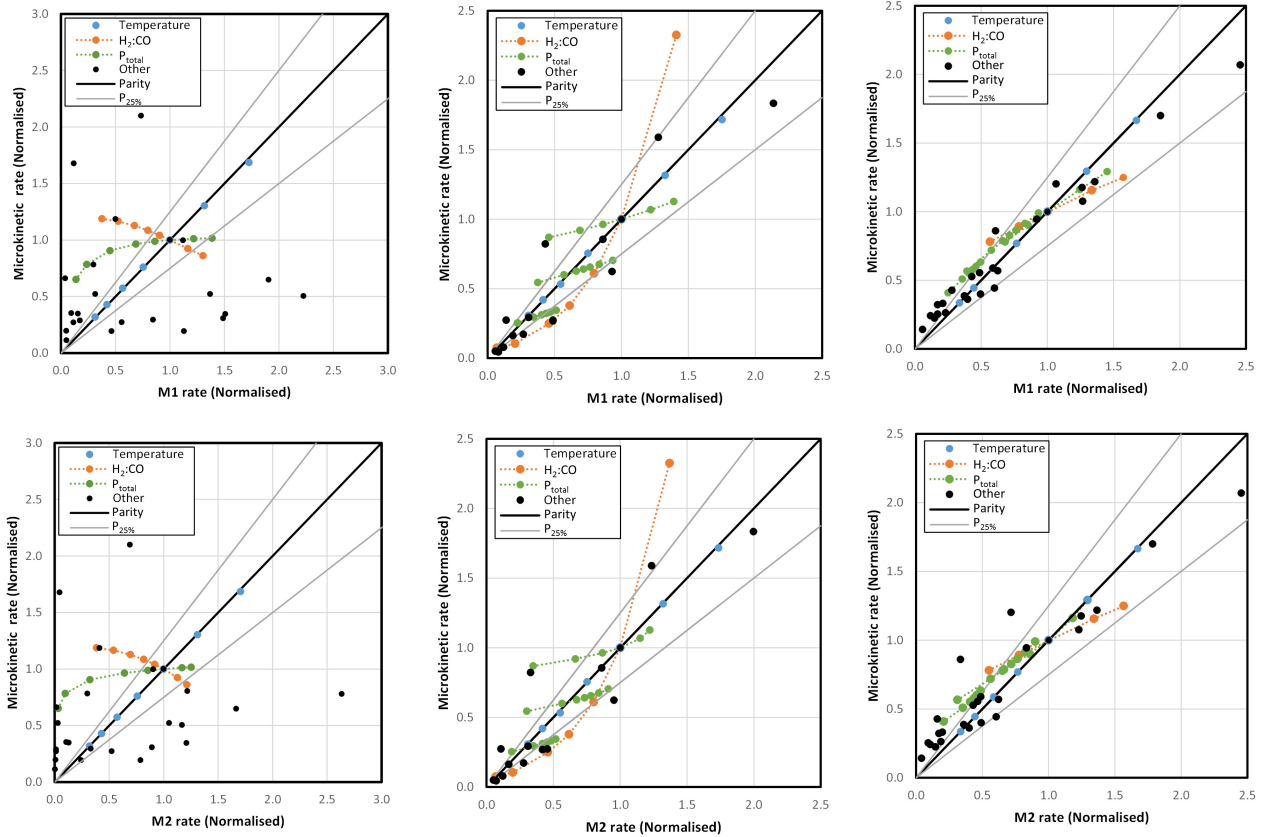


Fig. 8 Comparison between microkinetic calculated FTS rates and experimental summary macrokinetic models M1 (top) and M2 (bottom) for different scenarios: S1 (left); S2 (middle); S4 (right). All rates are normalized to a single condition ($T = 503$ K; $P_{total} = 20$ bar; Inlet $H_2:CO = 2$; $\chi_{CO} = 50\%$).

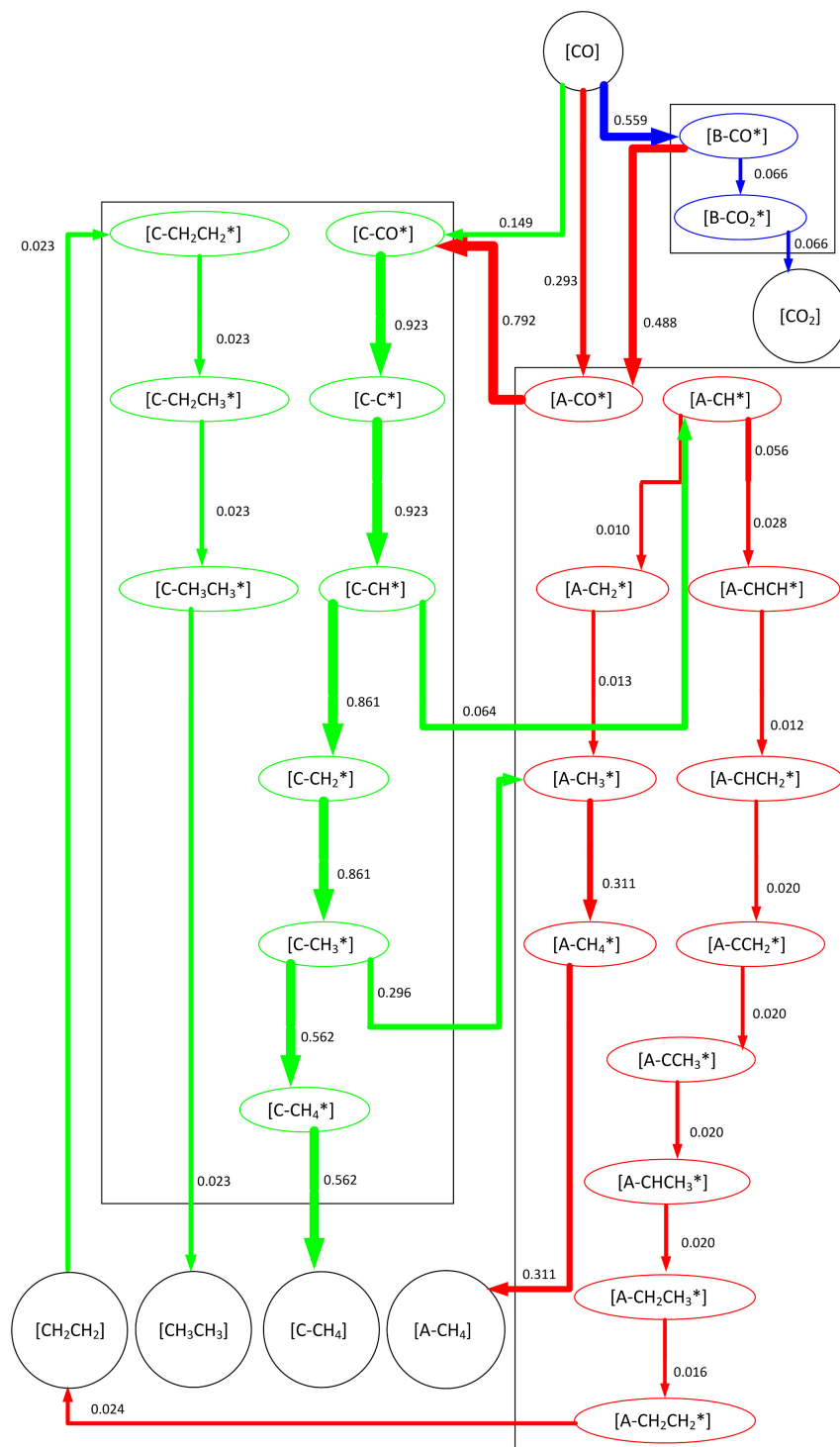


Fig. 9 The carbon atom reaction network for the multi-site Co microkinetic model under scenario S2 at the standard reference condition ($T = 503$ K; $P_{total} = 20$ bar; Inlet $H_2:CO = 2$; $\chi_{CO} = 50\%$). The arrow thickness is an indication of the scale of the rate and the C mol-% flow is indicated in the labels. The network was truncated at 1% of the total CO conversion rate.

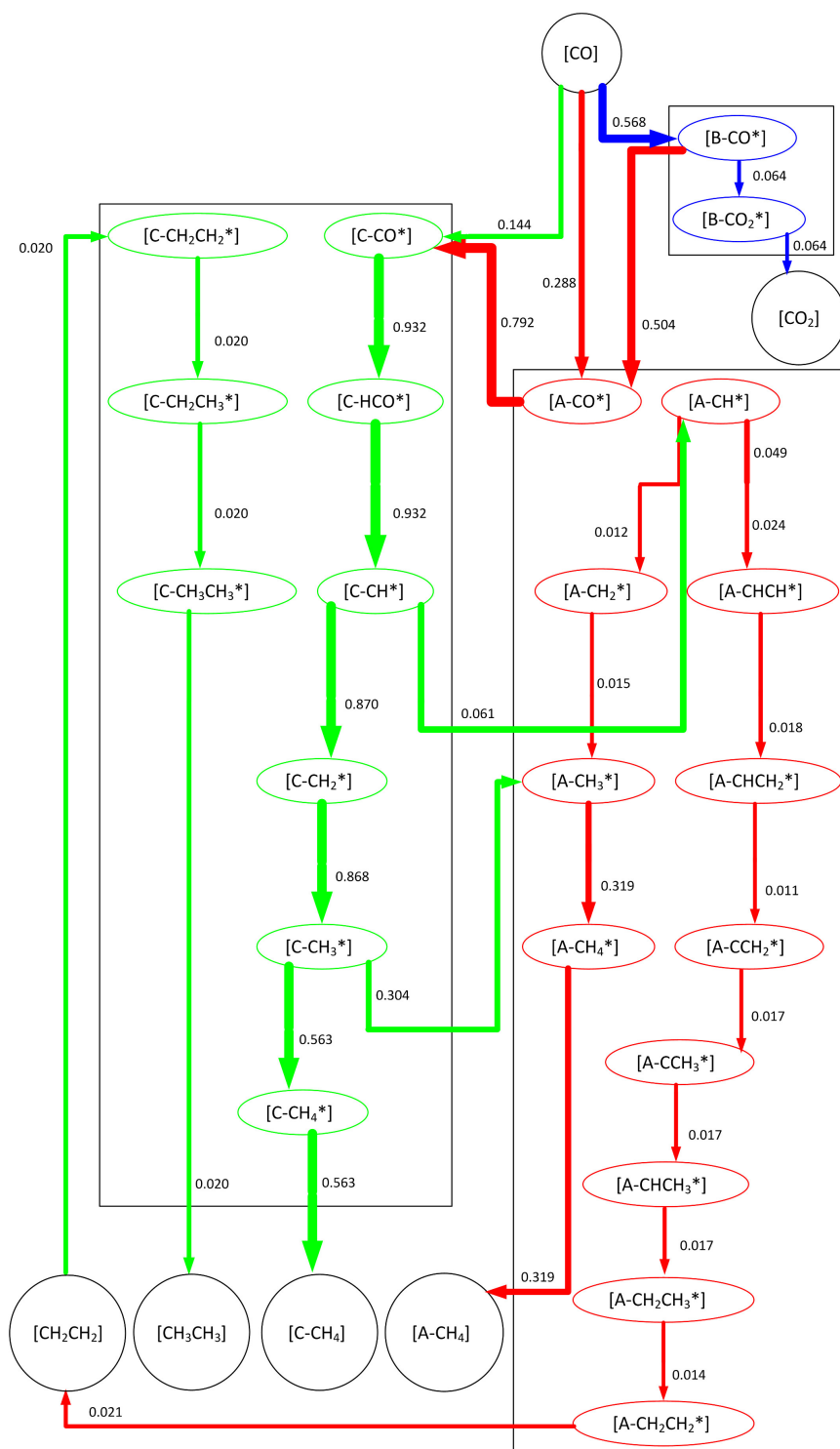


Fig. 10 The carbon atom reaction network for the multi-site Co microkinetic model under scenario S3 at the standard reference condition ($T = 503$ K; $P_{total} = 20$ bar; Inlet $H_2:CO = 2$; $\chi_{CO} = 50\%$). The arrow thickness is an indication of the scale of the rate and the C mol-% flow is indicated in the labels. The network was truncated at 1% of the total CO conversion rate.